Journal of Civil Structural Health Monitoring (2026) 16:106
https://doi.org/10.1007/s13349-026-01154-6

ORIGINAL PAPER

Low-power multi-channel strain sensing and QR-enabled shape visualization for digital-twin-enabled structural health monitoring

Suleman Khan[1] · Junyoung Park[2] · Jongwoong Park[3] · In-Ho Kim[4] · Jongbin Won[5]

Received: 5 February 2026 / Revised: 23 September 2026 / Accepted: 8 October 2026
© Springer-Verlag GmbH Germany, part of Springer Nature 2026

Abstract
Structural health monitoring (SHM) requires accurate and sustainable sensing systems to capture strain and displacement for evaluating the safety and performance of civil infrastructure. Conventional wired and wireless systems often suffer from high power demand, complex installation, or limited scalability, which restrict their long-term applicability. This study presents a low-power, multi-channel strain sensing and visualization system designed to address these limitations and to provide the sensing and visualization layer required for digital-twin-enabled monitoring. The system integrates three 24-bit strain sensing channels, a low-power microcontroller, and an electronic paper display that encodes measurements into a QR code. A mobile application decodes the QR code and uploads the data to a cloud database, where strain is transformed into displacement and visualized using a Building Information Modeling (BIM) framework. This approach provides lightweight data handling and shape visualization of the reconstructed deflection. Validation was performed through laboratory and large-scale experiments. In a simply supported beam test the displacement reconstructed at the validation load was within 0.04 mm, approximately 5%, of a laser displacement reference, while for a 5.45 m composite beam subjected to static loads up to 1300 kN the displacement reconstructed at its peak in the independent load case differed by 3.1% from the simultaneous reading of a reference displacement sensor.

Keywords Ultra-low power · Multi-strain measurement · Data visualization · Cloud database · Building information modeling (BIM)

1 Introduction

The unexpected failure of civil infrastructure has underscored the importance of systematic condition assessment to ensure safety and prevent social and economic losses. In recent decades, several catastrophic failures of bridges and buildings have highlighted the vulnerability of aging structures, which are often exposed to harsh environmental conditions, sustained traffic loads, and gradual deterioration of materials [1–4]. The collapse of the Sgt. Aubrey Cosens V.C. Memorial Bridge over the Montreal River in Latchford, Canada [5], serves as a representative example, where design deficiencies combined with insufficient inspection and maintenance led to sudden failure. Such incidents emphasize that the structural safety of bridges, railroads, dams, and other critical facilities must be quantitatively monitored throughout their life cycles [6, 7]. Structural health monitoring (SHM) has therefore become a critical area of research, aiming to provide continuous assessment

✉ In-Ho Kim
inho.kim@kunsan.ac.kr

✉ Jongbin Won
jbwon90@kict.re.kr

Suleman Khan
khansuleman444@gmail.com

1 Department of Smart City, Chung-Ang University, 84 Heukseok-ro, Seoul 06974, Republic of Korea

2 Universal Design & Novel Solution (UDNS) Co., Ltd, Seongnam 13558, Republic of Korea

3 Department of Civil and Environmental Engineering, Chung-Ang University, 84 Heukseok- ro, Seoul 06974, Republic of Korea

4 Department of Civil Engineering, Kunsan National University, 558 Daehark-ro, Gunsan 64150, Republic of Korea

5 Department of Structural Engineering Research, Korea Institute of Civil Engineering and Building Technology, Goyang 10223, Republic of Korea

Published online: 23 October 2026

Content courtesy of Springer Nature, terms of use apply. Rights reserved.

of structural integrity, guide maintenance decisions, and extend service life [8–12].

Among various indicators of structural performance, strain and displacement measurements are particularly important. Deflection is widely recognized as a global indicator of structural response, especially in bridges, where excessive deflection may indicate stiffness loss or cumulative damage [13–18]. Previous studies have shown that deflection is influenced by multiple factors, including corrosion of steel reinforcement, pre-stress loss, creep and shrinkage of concrete, and progressive crack growth. As these mechanisms evolve, deflection increases nonlinearly and accelerates the damage process, making deflection monitoring an effective early-warning tool. Consequently, long-term monitoring of strain and deflection has received growing attention in the SHM community. For example, Zhang et al. [19] highlighted the value of continuous deflection monitoring in detecting early-stage deterioration of bridge girders, while You et al. [20] demonstrated that deflection trends provide valuable insight into residual load-carrying capacity. Strain records are also used for structural behavior recognition outside bridge deflection. Tian et al. [21] derived a strain ratio index from fiber Bragg grating measurements to identify ice accumulation on wind turbine blades, and monitored response data have been combined with deep graph learning to predict the in-service performance of transportation infrastructure networks [22]. These studies indicate that long-term strain records serve not only for direct response assessment but also as input to data-driven models of structural behavior.

To measure strain and displacement, sensing technologies have undergone significant development [23–27]. Traditionally, wired sensors such as strain gauges and displacement transducers were widely used to obtain structural response data [28]. These systems transfer measurements through coaxial cables to a central acquisition unit, where the data is stored and processed. Although they provide reliable measurements, wired sensors have well-known shortcomings: their installation is time-consuming and expensive, they lack flexibility once installed, and the extensive cabling required introduces both maintenance and safety concerns. Furthermore, long-term exposure of cables in outdoor environments makes wired systems vulnerable to physical damage and signal degradation. These disadvantages limit the scalability of wired sensor networks for large or complex infrastructure.

With the rapid progress of wireless communication technology, wireless sensor networks (WSNs) have been introduced to replace conventional wired systems [29]. Wireless sensors integrate microcontrollers for calibration and processing and transmit data to a central server. Compared with wired systems, WSNs reduce installation effort and cost, enable more flexible deployment, and simplify maintenance. Additionally, distributed communication protocols allow nodes to preprocess data and minimize redundancy, improving memory efficiency and reducing data transfer requirements. These features make WSNs attractive for SHM, particularly in full-scale deployments where hundreds of sensors may be required. Several wireless sensing platforms have been developed and tested for SHM applications. The NARADA system, developed at the University of Michigan, provides 16-bit resolution but suffers from relatively low computational speed and data transmission rates, making it unsuitable for multi-channel strain acquisition in real time [30]. The G-link-200 platform from Microstrain is capable of measuring acceleration but has limited strain measurement capability and, like NARADA, requires a base station computer for data reception, which complicates deployment in the field [31]. The Xnode platform, developed at the University of Illinois, offers significant improvements with higher data transmission rates, long-range communication, and 24-bit measurement resolution [32]. It also supports multi-channel data acquisition. However, its dependence on base station computers and relatively high-power consumption limit its effectiveness for long-term monitoring. These examples illustrate that while wireless sensing technologies offer major advantages over wired systems, challenges in power efficiency, data reliability, and field deployment remain unresolved.

Given these limitations, alternative approaches have been explored to enhance SHM capabilities, among which strain visualization has gained recent attention. Strain visualization displays the response locally without continuous transmission, reducing power demand and simplifying interpretation. Mechanoluminescent (ML) materials were among the earliest techniques investigated for this purpose, as they emit light under mechanical loading and can visualize strain distribution across a surface [33–36]. Materials such as SrAl2O4:Eu, Dy (SAOED) demonstrated relatively high light intensity under daytime conditions [37]. However, ML materials are unsuitable for static monitoring because their luminescent response depends on the rate of applied stress rather than the magnitude, and their power efficiency is low.

To improve visualization, Xu and Jo [38] proposed integrating conventional strain gauges with electroluminescent (EL) panels. EL-based systems provided more stable visualization compared to ML, but their continuous active display required substantial power, significantly reducing efficiency for long-term monitoring. Moreover, strain was represented indirectly as panel intensity, requiring additional conversion devices, and the integration of EL panels increased overall cost.

Content courtesy of Springer Nature, terms of use apply. Rights reserved.

More recently, electronic paper display (EPD) technology has emerged as a promising solution for low-power strain visualization. Unlike emissive displays, EPDs mimic the appearance of printed ink by reflecting ambient light, which provides high visibility, wide viewing angles, and negligible standby power consumption. Early developments of EPDs include Gyricon [39], introduced in 1974, and microcapsule-based designs in 1998 [40]. Subsequent improvements in display technology, such as enhanced internal reflection, have led to commercially available panels with reliable performance [41–43]. Khan et al. [44] demonstrated a prototype single-channel system where strain data were encoded as QR codes and displayed on an EPD. This approach reduced power consumption, enabled long-term operation, and provided more accurate strain measurements compared to ML- and EL-based methods.

The term digital twin is used here with a defined scope. Kritzinger et al. [45] classified virtual representations by the way data move between the physical object and its counterpart: a digital model, in which the exchange is manual; a digital shadow, in which data flow automatically from the physical object to the virtual one; and a digital twin, in which the flow is automatic in both directions, so that the virtual object can also act on the physical one. In the experiments reported here the display was read either by an operator using the smartphone application or by a time-lapse camera whose images were decoded afterwards, so the path from the instrumented structure to the virtual model is not yet automated end to end. The system is therefore not claimed to realize a digital shadow. What it provides is the low-power sensing and visualization layer on which such a data flow is built: strain measurement, local encoding of the record, cloud storage, strain-to-displacement reconstruction and virtual representation. Automated image capture, bidirectional interaction, predictive simulation and life-cycle management lie outside the validated scope. The term is retained in the title and throughout the paper to identify the intended application, not to claim that those further functions have been implemented.

Building on these advancements, the present study proposes a multi-channel strain sensing and visualization system (MSVS) that integrates low-power strain measurement, QR code-based data encoding, and cloud-based Building Information Modeling (BIM) visualization. MSVS employs three 24-bit strain sensing circuits, an EPD for QR code generation, a smartphone application that decodes the QR codes and uploads the records to a cloud database, and a BIM-based framework that transform the strain measurements into displacement and visualize the deflection as a 3D shape. The system was validated through two experiments: a 2 m simply supported beam and a 5.45 m composite beam subjected to static loading.

The remainder of this paper is organized as follows: Sect. 2 describes the hardware and software development; Sect. 3 presents the cloud-based data management and BIM-based visualization framework; Sects. 4 and 5 provide laboratory- and large-scale validation; and Sect. 6 concludes the study.

2 Development of MSVS

This section describes the development of the proposed MSVS, including both hardware and software aspects. The hardware development focused on two critical requirements for long-term SHM applications: low-power operation and high-resolution strain measurement. MSVS hardware consists of three major components: (i) a power management circuit, (ii) strain sensing circuits, and (iii) an EPD for QR code–based data visualization, as shown in the block diagram of Fig. 1. Each component is described in detail in the following subsections. The final subsection describes the embedded firmware, while the cloud-based data management and BIM-based visualization are presented in Sect. 3.

2.1 Power management circuit

A power management circuit (PMC) was designed to enable efficient long-term monitoring by controlling the battery supply to the microcontroller unit (MCU) and other power-consuming devices, including the EPD and analog-to-digital converters (ADCs). The functional block diagram of the PMC is shown in Fig. 2. The nRF52840 [46] was selected as the MCU due to its large on-chip static random-access memory (SRAM, 256 kB), which is critical for generating and storing the 400 × 400 pixel QR code (requiring 178 kB, or 69.5% of available memory), and its low active current consumption (14 mA).

The PMC supports two activation events: a real-time clock (RTC) and a manual push button. The RTC (DS3231) [47] generates an active-low logic signal at user-programmable intervals, while the push button allows activation on demand. These signals are combined using a configurable logic gate [48]. When either the RTC or the push button is activated, the gate outputs a low signal. An inverter [49] converts this to a high signal that enables the voltage regulators [50], which provide a stable 3.3 V supply to the circuit.

Once the MCU begins processing, it latches the signal from the inverter to maintain the power supply throughout the sensing and visualization sequence. After completing the cycle, the MCU releases the latch to return the system to a low-power state. A digital load switch [51] and a D-type latch [52] are used to support this power control mechanism. All components used in the PMC are selected for their

Content courtesy of Springer Nature, terms of use apply. Rights reserved.

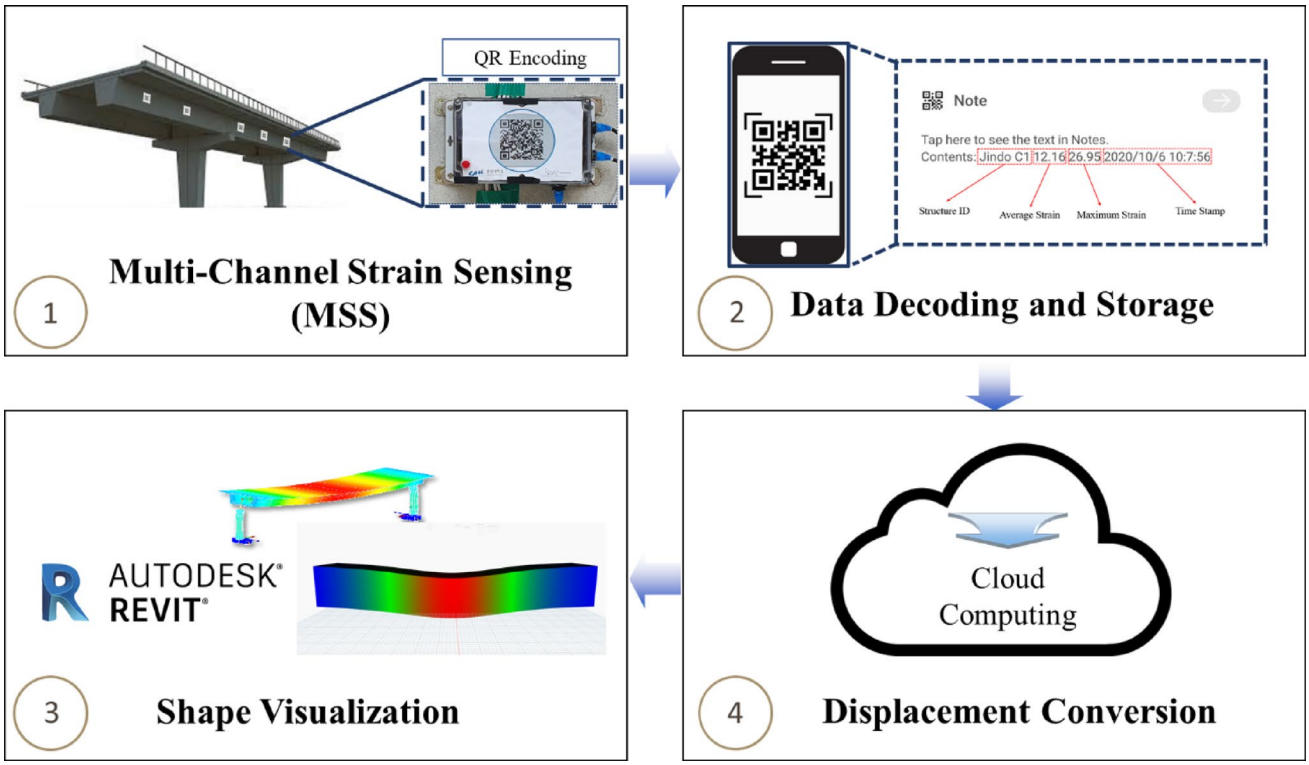
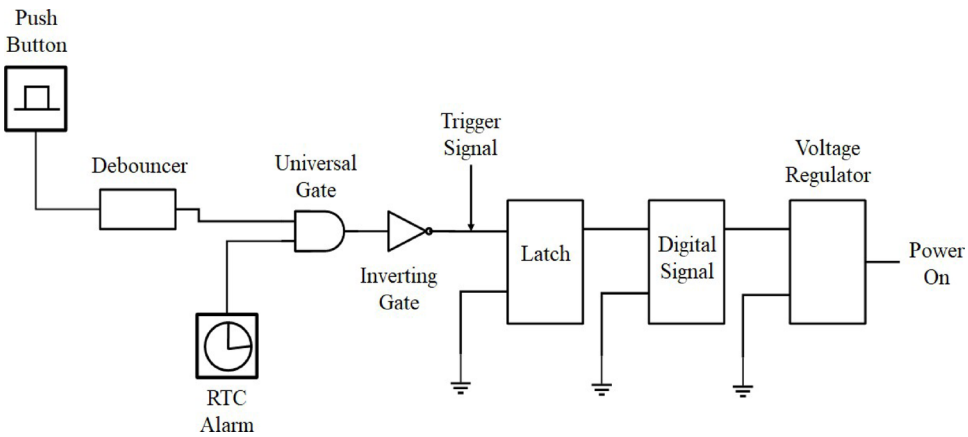


Fig. 1 Block diagram of developed MSVS

Fig. 2 Functional block diagram of PMC



low power consumption, ensuring suitability for long-term SHM applications.

2.2 Multi-channel strain sensing

MSVS acquires high-fidelity strain data using half-bridge strain circuits and 24-bit ADCs. The half-bridge configuration employs two strain gauges to achieve balance and minimize drift. Differential voltages from the half-bridge are measured by the ADS1220 [53], a 24-bit low-power ADC. Figure 3 shows the implemented circuit, where IN and IP represent the negative and positive terminals of the bridge output. Both IN and IP are biased at half of the excitation voltage (VCC). Two 10 kΩ resistors are used to reduce power consumption and maintain balance. The voltage at IP varies with the resistance change of the strain gauges, while IN remains at half of VCC. The differential voltage is first passed through an RC low-pass filter (R = 10 kΩ, C = 1 μF), providing a cut-off frequency of 15.9 Hz, before being digitized by the ADC.

The ADS1220 includes internal noise filtering at 50–60 Hz, supports multiple conversion modes, and was operated in single-shot conversion mode at a data rate of 20 samples per second (SPS). Conversion noise and quantization in the acquisition chain set a floor on the achievable strain precision that is independent of the other error terms

Content courtesy of Springer Nature, terms of use apply. Rights reserved.

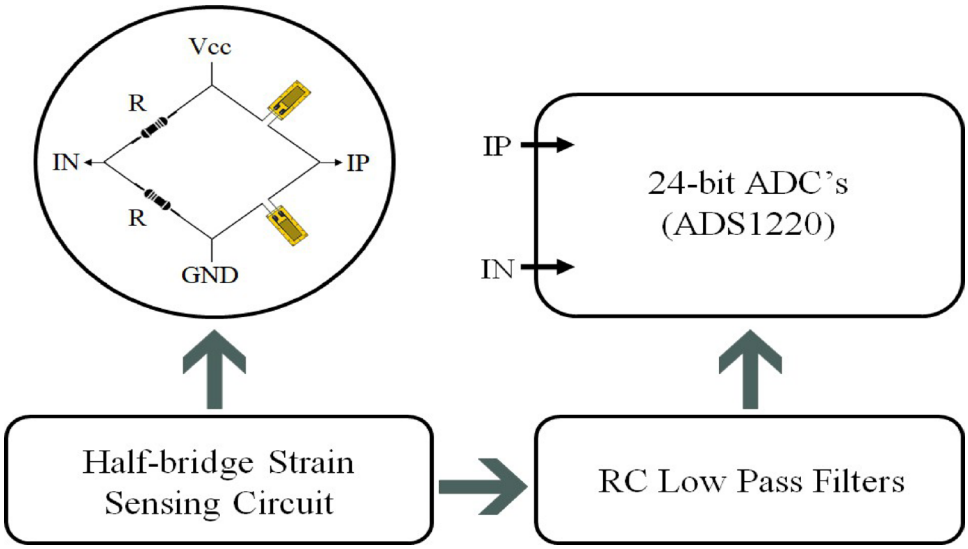


Fig. 3 Strain sensing circuit

discussed in Sect. 4. Since each ADS1220 offers two differential channels, two ADCs were used to measure three differential channels in MSVS.

The differential voltage V_{diff} is computed from the raw ADC output as follows:

$$V_{\text{Diff}} = \frac{ADC_{val} \times V_R}{FR} \tag{1}$$

where ADC_{val} is the raw value obtained from ADC, V_R is the internal reference voltage (2.048 V) to programmable gain value ratio, and FR is 2^{23}, the number of codes spanning the positive full-scale input of the ADC, whose 24-bit output is a two's complement code [53].

The strain ϵ is then calculated as:

$$\epsilon = \frac{4}{V_{CC} \times GF} \times (V_{Diff} - V_{Offset}) = CF \times (V_{Diff} - V_{Offset}) \tag{2}$$

where GF is the gauge factor, V_{offset} is the initial offset voltage used to balance the bridge, and CF is the calibration factor defined by GF and the excitation voltage V_{CC}. For a gauge factor of 2, CF equals 606,100 $\mu\epsilon/V$. Because the differential bridge output is of the order of one millivolt at the strain levels encountered in these tests, the calibration factor is applied per millivolt of bridge output throughout this paper, so that the value above is equivalently 606.1 με/mV. The gauges used in Sects. 4 and 5 have a gauge factor of 2.1, for which Eq. (2) gives 577.2 με/mV at the nominal excitation of 3.3 V. The value of 576 με/mV adopted in those tests corresponds to a measured excitation of 3.307 V and was carried over from the single-channel implementation that preceded this work [44].

During operation, MSVS samples at 20 SPS over a short window at each activation, averages each channel, and uses the result for QR encoding and visualization. The window is configurable and was set to 200 samples per channel, approximately 10 s, in both the laboratory test of Sect. 4 and the large-scale test of Sect. 5, so that reading the three channels in sequence occupies about 30 s of the 39 s sensing mode described in Sect. 2.3.

Table 1 Idle-state current consumption of MSVS components

Device	Current Consumption
ZS-042 (DS3231 RTC module)	200 μA
SN74AUP1G58 (Universal gate)	0.9 μA
SN74LVC1G04 (Inverting gate)	10 μA
SN74LVC1G373 (D-type latch)	10 μA
TPS22860 (Digital switch)	0.1 μA
MCP1725 (Voltage regulators)	120 μA
Total	341 μA

2.3 Power consumption analysis

The power consumption of MSVS was analyzed in both idle and sensing modes to evaluate its suitability for long-term operation. Table 1 summarizes the current consumption of MSVS components during idle mode. In this state, MSVS consumes only 0.34 mA while maintaining the QR code display for data acquisition. When activated, MSVS enters sensing mode, during which the current consumption increases to 36.63 mA for a duration of 39 s.

The value of 36.63 mA is the total current drawn on the battery rail, measured while the system executed one complete sensing and display cycle. It therefore aggregates the microcontroller, the two ADCs, the display driver and the supporting logic across the 39 s window, over which those blocks are not all active at the same time. Resolving the figure by functional block would require the supply of each block to be instrumented separately, or the rail current to be

Content courtesy of Springer Nature, terms of use apply. Rights reserved.

sampled and gated against the acquisition, QR generation and display refresh phases of the sequence. That measurement was not performed in this study and is identified as a refinement for further characterization of the platform. The per-device figures in Table 1, by contrast, were measured individually in the idle state.

The average current consumption I_{avg} can be estimated assuming one sensing event every 30 days, using:

$$I_{avg} = \frac{I_{idle} \cdot (T_{total} - T_s) + I_{sensing} \cdot T_s}{T_{total}} \quad (3)$$

where I_{idle} is the idle current (0.34 mA), $I_{sensing}$ is the sensing current (36.63 mA), T_s is the sensing duration (39 s), and T_{total} is the total time in 30 days ($30 \times 24 \times 3600$ s). Substituting values yields an average current consumption of approximately 0.34 mA.

The expected battery life is then calculated as:

$$BatteryLife = \frac{Capacity\,(mAh)}{I_{avg}} \times 0.8 \quad (4)$$

where a compensation factor of 0.8 is applied to account for environmental conditions and battery degradation. With a battery capacity of 30,000 mAh and one sensing event per month, MSVS is expected to operate for approximately 8.05 years. This figure is an idealized charge-budget estimate obtained from the measured currents and the rated capacity under the stated assumptions, rather than a demonstrated field lifetime.

The compensation factor of 0.8 in Eq. (4) follows the battery degradation model of Hashmi et al. [54]. In that model the capacity available at any point in service is expressed as the rated capacity reduced by a degradation term that takes the greater of two contributions, one proportional to the number of equivalent full depth-of-discharge cycles performed relative to the rated cycle life of the cell, and one proportional to elapsed time relative to its calendar life. End of life is reached when the available capacity has fallen to 80% of the rated value, which is the origin of the factor adopted here. The two contributions are not of equal weight for the present application. MSVS discharges its cell monotonically and performs no charge and discharge cycling of consequence, so the cycle term is negligible and degradation is governed by the calendar term, which accumulates with elapsed time irrespective of use and is itself sensitive to the ambient temperature at the installation. Applying the factor to the rated capacity throughout the calculation is conservative, since the available capacity falls from the rated value towards 80% of it over the service period rather than remaining at that lower bound. Because the service life given by Eq. (4) scales linearly with this factor, a value of 0.6 would give 6.0 years and a value of 0.9 would give 9.1 years. These are illustrative sensitivity cases rather than measured values. No long-term battery aging test was carried out in this study, so the factor is adopted as a literature-based assumption on usable capacity for the charge-budget estimate rather than as a coefficient identified experimentally for the cell used here.

Table 2 Predicted service life as a function of activation interval

Activation interval	Average current (mA)	Service life (years)
10 min	2.699	1.02
1 h	0.733	3.74
6 h	0.406	6.76
1 day	0.356	7.69
7 days	0.342	8.00
30 days (adopted)	0.341	8.05
90 days	0.340	8.05

The 30-day activation interval was selected because the deterioration mechanisms that motivate deflection monitoring, among them creep, shrinkage, prestress loss and corrosion of reinforcement, develop over weeks to months, so a monthly record is a reasonable low-duty design scenario for following that trend. It is also compatible with routine inspection practice. It is not claimed that a monthly reading is sufficient for every deterioration mechanism or site condition, since the interval required depends on the response being monitored, the loading environment and the objective of the monitoring. Table 2 gives the average current and the resulting service life obtained from Eqs. (3) and (4) for other intervals. Because the 39 s sensing event is short relative to the interval, the idle current dominates the average for any interval longer than about one day, and the predicted service life changes little between 90-day and daily activation. Service life falls more steeply once the interval becomes shorter than one hour, where the sensing event ceases to be a small fraction of the cycle. MSVS can therefore support daily activation at a cost of approximately 5% of service life, or hourly activation with a service life near 3.7 years, if an application requires finer temporal resolution. For shorter intervals either a larger cell or an ambient energy source would be needed, since service life scales linearly with capacity at fixed average current.

2.4 QR code display

A 7.5-inch high-definition black-and-white EPD [55] was used to display QR codes containing the sensing data. The display offers a resolution of 880 × 528 pixels and a viewing angle greater than 170°, making it suitable for presenting detailed information.

To encode the strain measurements together with time information, the three-channel record was encoded as a version 3 QR code at error correction level L, rendered at a

Content courtesy of Springer Nature, terms of use apply. Rights reserved.

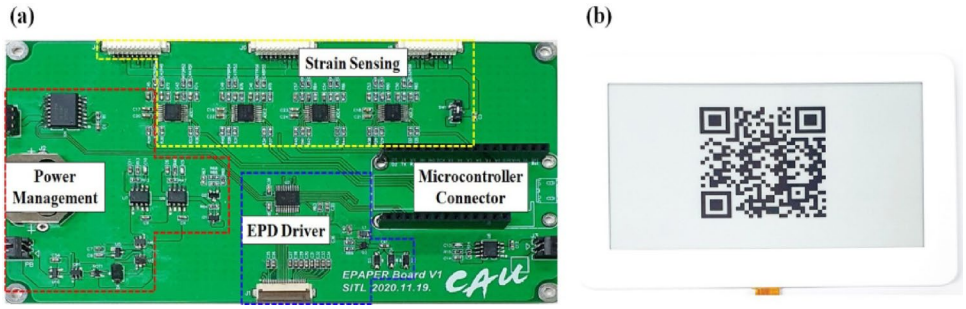


Fig. 4 Developed MSVS hardware: **a** Developed PCB, and **b** EPD

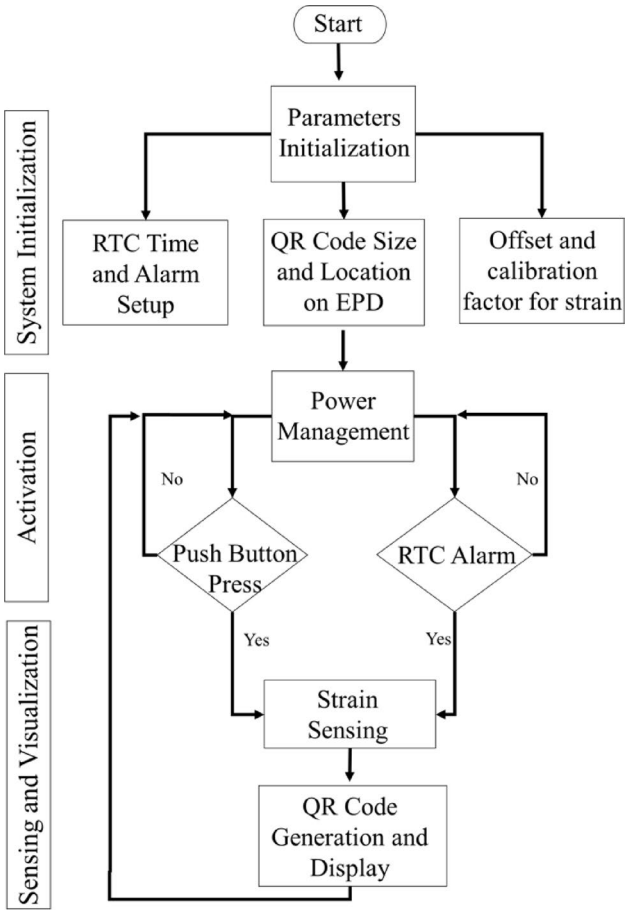


Fig. 5 Developed software flow for MSVS

resolution of 400 × 400 pixels. At this level version 3 supports a maximum data capacity of 53 bytes, which was sufficient to store the structure ID, three-channel strain measurements, and time information. The data were organized as 4 bytes for the structure ID, 12 bytes for time, and up to 6 bytes per strain channel, resulting in a total of 38 bytes including formatting space. The MCU generated the QR code modules (29 × 29), surrounded them with a quiet zone two modules wide to form a 33 × 33 array, and upscaled the array to 400 × 400 pixels to improve recognition reliability during acquisition. However, displaying a 400 × 400 QR code required 178 kB of SRAM (69.5% of the 256 kB pool), including the driver's frame and auxiliary buffers. This constraint highlights the importance of efficient memory management to ensure sufficient resources for additional processing tasks. Overall, the integration of a high-resolution EPD with version 3 QR code encoding offers an efficient and practical method for visualizing and sharing multi-channel strain data with time stamps, while maintaining the low-power operation of MSVS (Figs. 4, 5, 6, 7, and 8).

The choice of version 3 balances payload capacity against decoding reliability, and the memory cost of the two considerations is not symmetric. The array holding the module states is a minor allocation, since the 33 × 33 array occupies approximately 1 kB and a move to version 4 would enlarge it to 37 × 37 with the same quiet zone, an increase below 0.3 kB. The dominant allocations are fixed by the rendering resolution rather than by the version: the upscaled 400 × 400 bitmap accounts for approximately 156 kB and the packed single-bit buffer transferred to the panel for a further 20 kB, which together with the driver buffers make up the 178 kB reported above. Raising the version therefore does little to relieve the memory constraint, because that constraint originates in the display resolution. The binding limitation is instead the rendered size of an individual module. At the 400 × 400 resolution used here the version 3 array assigns approximately 12 pixels to each module, whereas version 4 would assign approximately 11 and version 5 approximately 10, progressively reducing the tolerance to camera resolution, focus and standoff distance during field acquisition. Version 3 was adopted for the three-channel record because it is the smallest version that carries the 38 byte record in byte mode: version 2 offers 32 bytes at level L, whereas the 53 bytes of version 3 accommodate the structure identifier, the three strain channels and the time stamp with a margin of 15 bytes, and at a fixed rendering resolution the smallest adequate version gives the largest module. A version 4 build of the firmware, with 78 bytes at level L, serves configurations of up to eight channels at the cost of a slightly smaller module, and the enclosure photographed in the inset of Fig. 9 displays a version 4 test code of this kind, with eight fixed values. Three alternatives were considered before the configuration was fixed. Raising the error

Content courtesy of Springer Nature, terms of use apply. Rights reserved.

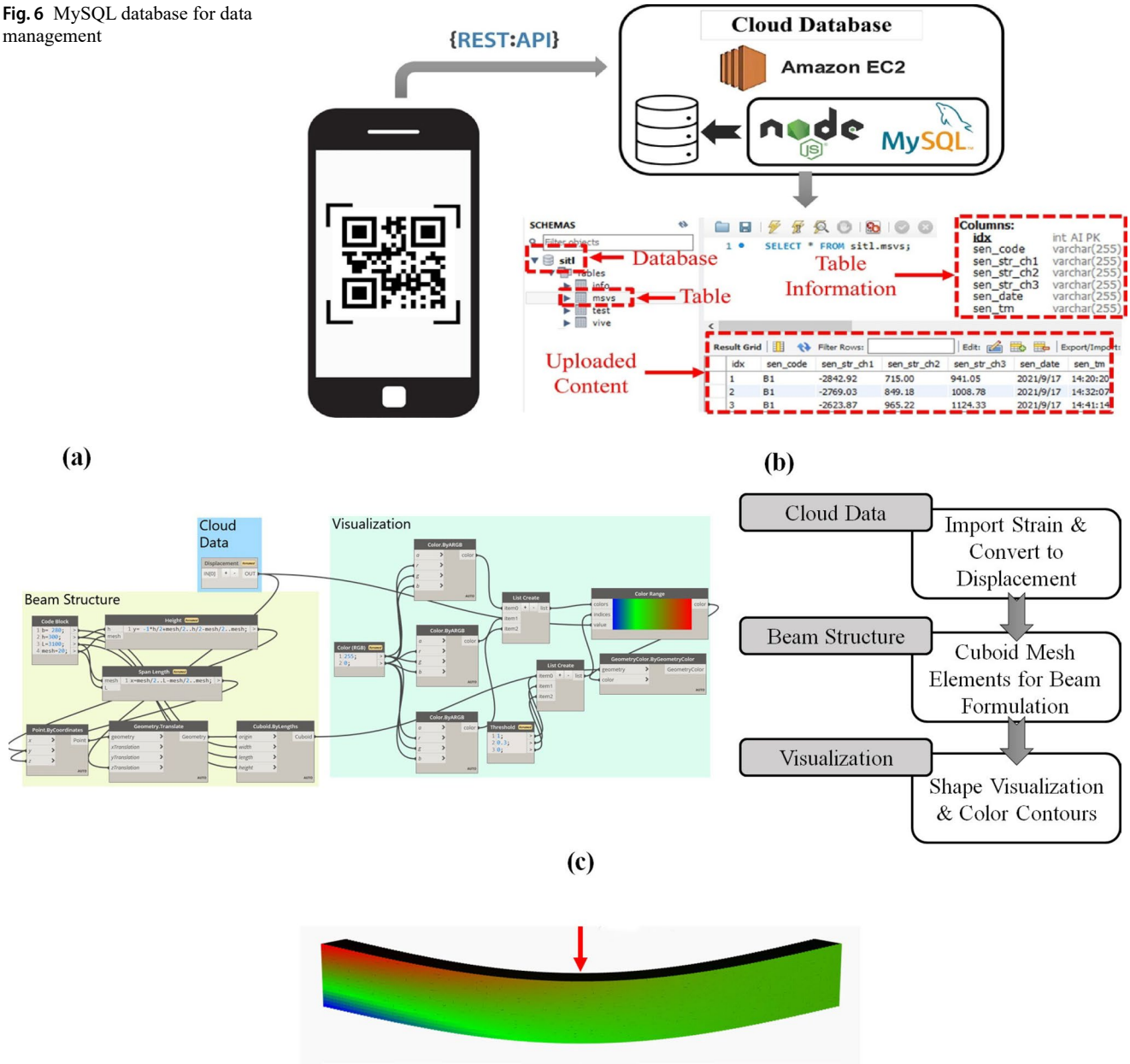


Fig. 6 MySQL database for data management

Fig. 7 Developed BIM-based visualization framework: **a** dynamo blocks, **b** Flow diagram, and **c** visualized deflection

correction level from L to M at the same version leaves a capacity of 42 bytes, which still carries the present record but not a fourth channel, and it was not adopted because the code is read at close range under controlled conditions rather than from a degraded surface. Distributing the record over two codes shown on successive activations was rejected because a complete record would then depend on both codes being captured, doubling the number of site visits required. Reducing the rendered resolution below 400×400 would release memory but shrinks the module in the captured image, which works against the recognition reliability that the upscaling is intended to provide.

The behavior of the display under field conditions also requires consideration. Because the panel is reflective rather than emissive, its legibility improves with ambient illumination and is retained in direct sunlight, where emissive displays lose contrast. The corresponding limitation is the absence of a backlight, so acquisition must take place in daylight unless the scanning device supplies its own illumination. Operation is bounded by the temperature range specified for the panel [55], and the refresh becomes slower and less uniform towards the lower end of that range. Since the panel is refreshed only once per activation event, a slower refresh has little consequence for the measurement

Content courtesy of Springer Nature, terms of use apply. Rights reserved.

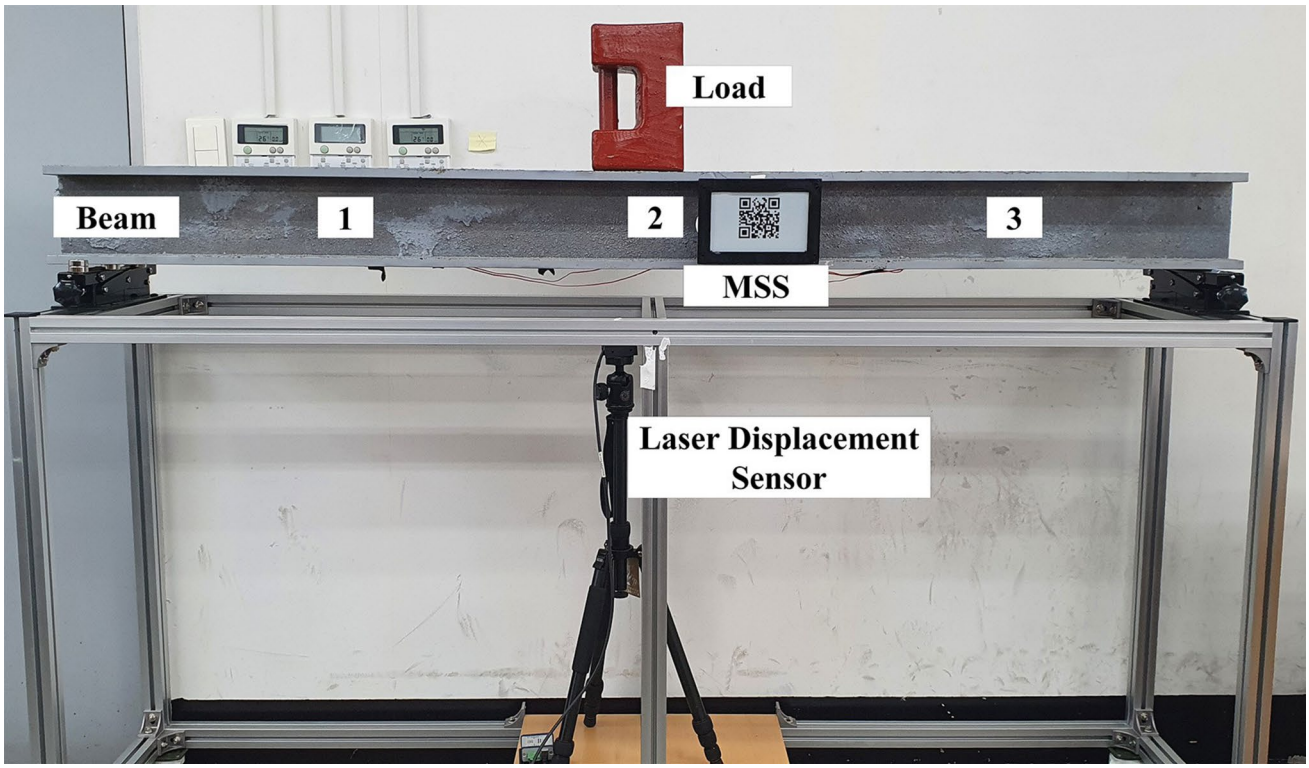
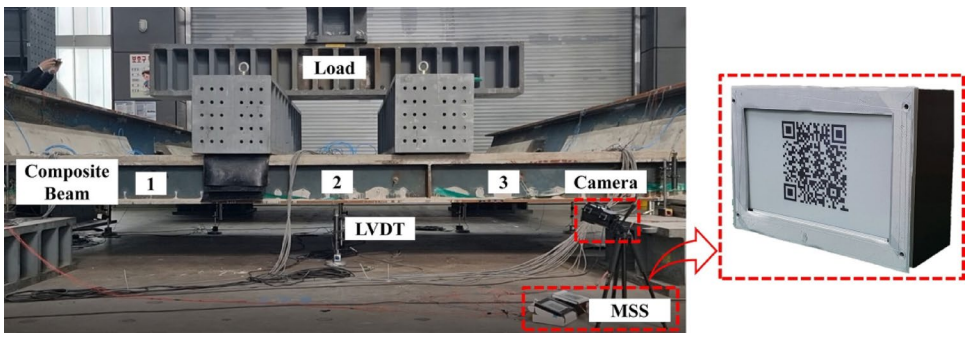


Fig. 8 Laboratory scale experimental setup

Fig. 9 Real-world scale experimental setup



cycle. Retention of a static image over a long interval can leave faint residual contrast, which the full black-and-white refresh performed before each new code removes. For field installation an enclosure rated to at least IP65, fitted with an ultraviolet-resistant window, is recommended to limit dust accumulation and moisture ingress. These measures follow from the device specification and from general outdoor practice; extended outdoor exposure was not evaluated in this study and is included in the planned field validation.

2.5 Developed MSVS hardware

The developed MSVS hardware serves as the core unit of the system, responsible for acquiring strain data from Wheatstone bridges and displaying the encoded QR code on the EPD. The circuit was fabricated on a 150 × 80 mm printed circuit board (PCB), providing a compact and efficient form factor suitable for long-term and remote sensing applications (see Fig. 4). The hardware is organized into four functional blocks: the three components introduced above together with the microcontroller that coordinates them, each performing a specific role.

The microcontroller block is based on the nRF52840, a 32-bit ARM Cortex-M4 device operating at up to 64 MHz, which manages all system operations including strain data acquisition, QR code generation, and power management. The strain sensing block interfaces with Wheatstone bridge circuits and incorporates RC low-pass filters, and 24-bit ADCs with integrated programmable gain amplifiers (Sect. 2.2) to ensure precise digital conversion of strain signals. The power management block includes the RTC, logic ICs, and a digital switch to minimize power consumption

Content courtesy of Springer Nature, terms of use apply. Rights reserved.

by enabling periodic activation (e.g., every 30 days) and controlling power delivery to the MCU and EPD, thereby ensuring extended battery life. Finally, the EPD driver block connects the MCU to the 7.5-inch black-and-white EPD, with a resolution of 880 × 528 pixels and a viewing angle exceeding 170°, ensuring reliable QR code display for data acquisition. These integrated blocks form a compact and low-power MSVS hardware platform capable of reliable multi-channel strain sensing and efficient data visualization for long-term SHM applications.

2.6 Developed integrated software for MSVS

An integrated software framework was developed to coordinate the operation of MSVS. The software operates in three stages: system initialization, activation and sensing, and visualization, as illustrated in the flow diagram in Fig. 5.

During system initialization, the parameters of all devices are configured. The EPD is set with its center position and the QR code resolution (400 × 400 pixels). The ADCs are initialized with calibration factors and offset values to enable conversion from voltage to strain, and the RTC is programmed with the time, date, and alarm interval. Once initialization is complete, the system enters a low-power standby mode.

When activated by either the RTC alarm or the push button, MSVS powers on and enters the sensing stage. In this stage, three-channel strain data are acquired and processed. Immediately afterward, the visualization stage encodes the measured data into a QR code, which is displayed on the EPD. The system then shuts down again, returning to standby mode until the next activation signal is received. The code remains on the display until the following activation, so its acquisition is independent of the moment of measurement. An inspector can photograph it during a routine visit, or a fixed camera can be triggered on the same schedule as the sensing event, without the unit needing to be aware of when the reading is taken. Both routes were used in this study, the manual scan in the laboratory test of Sect. 4 and the time-lapse camera in the large-scale test of Sect. 5. In neither case was the image captured and uploaded automatically, so the path from the display to the database is not demonstrated end to end here.

Because the EPD retains the QR image with virtually zero hold power, standby draw arises mainly from the RTC and the voltage regulator, with a minor contribution from the logic ICs, yielding substantial energy savings. This integrated framework therefore ensures reliable operation of MSVS while maintaining ultra-low power consumption for long-term SHM applications.

3 Development of data management system and BIM-based visualization framework

A cloud-based data management system was implemented to store the strain responses obtained from MSVS. A smartphone application was developed to serve as a bridge between MSVS and the cloud database, enabling reliable data transfer and storage. In addition, a simplified 3D visualization model was created within a BIM environment to represent deflection derived from the strain data. While the framework was implemented in Revit with Dynamo, it functions as a parametric visualization tool rather than a full BIM system, but is sufficient for the deflection visualization reported here.

3.1 Cloud-based data management system

The strain and time information encoded in QR codes is managed through a cloud database. An Android application was developed to scan and decode QR codes before uploading the decoded data to the cloud. Data transfer is handled via a Representational State Transfer application programming interface (REST API), which posts the information in JSON format to a specified table on the server. Amazon AWS Elastic Compute Cloud (EC2) [56] was used to host the cloud server, and MySQL [57] was employed as the open-source database for data storage.

The Android application [58] utilizes an open-source QR code scanning library [59] to extract the encoded information, converts the results into JSON objects, and uploads them to the database using the Volley HTTP library [60]. Permissions for camera and internet access were configured within the app. The database schema consists of seven variables (index, ID, three-channel strain measurements, date, and time). Node.js [61] was deployed on the server to host the REST API and manage the data insertion process. This framework (Fig. 6) ensures that MSVS data can be reliably uploaded, stored, and accessed for subsequent visualization.

Two aspects of this data path require attention before unattended deployment. The first is protection of the record in transit and at the server. The transfer described above should be carried out over a channel secured by transport layer security, and the interface should accept records only from registered devices presenting a valid credential, so that measurements cannot be read or substituted by a third party. The second is the behavior of the application when connectivity is unavailable, which is common at bridge sites. Decoded records should be written to persistent storage on the handset at the moment of scanning and transmitted when a connection next becomes available, so that a reading is not lost to a transient network failure. A distinction

Content courtesy of Springer Nature, terms of use apply. Rights reserved.

should be drawn between the two ways a record can be lost. Local caching protects a record once the code has been photographed and decoded, but it cannot recover a display update that was never photographed, because the following activation overwrites the code. Retaining a short history of records in non-volatile memory on the unit, or carrying a sequence number in the payload so that a missing record can be detected, is noted as a further improvement. The validation reported in this paper exercised the acquisition, transfer and storage path rather than its security properties, which were not evaluated. The measures above are therefore stated as requirements for unattended field deployment rather than as results of this study.

3.2 BIM-based visualization framework

A parametric 3D visualization framework was developed in the Revit–Dynamo environment to display structural deflection from the cloud-stored strain data. The workflow is illustrated in Fig. 7 and consists of three blocks: cloud data, beam structure, and visualization.

The "Cloud Data" block imports the three-channel strain measurements from the MySQL database through a Python script embedded in Dynamo. The strain data are converted into displacement using the assumed mode method proposed by Park et al. [62]. The linear relationship between strain and displacement is expressed as:

$$\{u\}_{x_i} = \alpha \Phi_{i\times j} \Psi^{+}_{j\times n} \{\epsilon\}_{x_n} \tag{5}$$

where $\{u\}_{x_i}$ is the set of displacements estimated from the measured strains $\{\epsilon\}_{x_n}$, $\Phi_{i\times j}$ is the displacement mode shape, $\Psi_{j\times n}$ is the strain mode shape, "+" denotes the pseudo-inverse, and α is a scale factor used for calibration.

The scale factor in Eq. (5) is not fitted to each load step but follows from the formulation of Park et al. [62]. In that work the displacement and strain responses are each expanded over a finite set of modes, the modal coordinate is recovered from the measured strains through the pseudo-inverse of the strain mode shape matrix, and the displacement is obtained by substituting that coordinate into the displacement expansion. For a simply supported beam with sinusoidal mode shapes the resulting transformation carries the physical group L squared divided by y pi squared, in which L is the span and y is the distance from the neutral axis to the instrumented fiber. Once the mode shapes are normalized, the scale factor represents that group, so its value is set by the span and by the position of the neutral axis rather than by the applied load. This is why it differs between the two beams reported here. Park et al. [62] identify the position of the neutral axis as the critical unknown in this relationship, noting that it is difficult to establish for composite sections and that calibration against an accurate reference such as an LVDT is therefore required when only strain is measured. Their own method avoids that calibration by combining strain with acceleration and adjusting the factor in the frequency domain until the displacement spectra from the two sources agree. MSVS carries no accelerometer, so this calibration-free route is not available and the factor was instead established by reference measurement, using the laser displacement sensor in the laboratory test and the LVDT in the large-scale test. Because the factor is established in this way, the reference instruments are not fully independent of the reconstructed displacement, and the comparisons reported in Sects. 4 and 5 should be read with that dependence in mind. A factor established by reference measurement also absorbs any uniform scale error in the measured strain, such as one arising from gauge installation or the bridge configuration, so the adopted value need not coincide exactly with the geometric group. The two are distinguished in Eqs. (7–9) below as the geometric coefficient k_{geo} and the effective coefficient k_{eff}. In each test one of the two load cases is therefore used to fix the factor and the other provides the independent comparison, namely the 20 lb and 40 lb cases in Sect. 4 and Case 1 and Case 2 in Sect. 5. The effective coefficient of approximately 56,300 microstrain per meter adopted for the composite beam corresponds through the relationship above to a neutral axis approximately 0.17 m from the instrumented fiber. For a member that remains linear elastic and satisfies small deflection theory the factor is independent of load magnitude, since it derives from the section geometry and the assumed shape rather than from the applied load. Its variation across load levels was not characterized experimentally in this study. Load independence would not hold if the section approached yield or if the support condition changed in service, in which case the factor would require periodic recalibration against a reference measurement.

Setting this relationship out explicitly for the configuration used here, the one-term half sine displacement field, the strain it implies at a measurement position, and the amplitude recovered from the measured strains are

$$w(x) = q\sin\left(\frac{\pi x}{L}\right) \tag{6}$$

$$\epsilon_i = -10^6 y w''(x_i) = k_{geo} q \psi_i \tag{7}$$

$$q = \frac{\psi^{T}\epsilon}{k_{eff}\psi^{T}\psi} \tag{8}$$

where w(x) is the deflected shape and q is its amplitude at mid-span, L is the span, y is the distance from the neutral

Content courtesy of Springer Nature, terms of use apply. Rights reserved.

axis to the instrumented fiber, and x denotes position along the span. Equation 7 is the Euler–Bernoulli curvature relation applied to Eq. (6), with strain expressed in microstrain, in which ψ is the assumed shape sin(πx/L) evaluated at the measurement positions and k_{geo} is the geometric coefficient $10^6 y\pi^2/L^2$, which carries the unit of microstrain per meter. In Eq. (8), ε is the vector of measured strains in microstrain, ψ is the vector of shape values at the same positions, and the superscript T denotes the transpose, so that the expression is the equal-weight least squares estimate of the amplitude, written with the effective coefficient k_{eff} defined below, which takes the place of k_{geo} in the reconstruction. The scale factor α in Eq. (5) corresponds to the reciprocal of k_{eff} and carries the unit of meters per microstrain. Written in this form the geometric strain-per-displacement coefficient is separated from the modal fitting step, so that the coefficent reported for each beam carries an explicit unit rather than acting as a multiplier on an intermediate quantity of the processing.

The coefficient applied in the tests is not computed from k_{geo}, because the position of the neutral axis is difficult to establish for composite sections, as noted above, and because a uniform scale error in the measured strain enters the reconstruction in the same way as an error in y. It is replaced by an effective coefficient k_{eff}, calibrated from a single reference displacement w_{ref} measured at mid-span, where ψ equals one, together with the strain vector ε_{ref} recorded at the same time:

$$k_{\text{eff}} = \frac{\psi^{\mathrm{T}} \epsilon_{\text{ref}}}{\psi^{\mathrm{T}} \psi w_{\text{ref}}} \tag{9}$$

which follows from Eq. (8) by setting q equal to w_{ref}. Equation 8 is then applied with k_{eff} to every other record of the same test. The reference cases are the 20 lb case in Sect. 4 and Case 1 in Sect. 5, so the coefficients reported in those sections are values of k_{eff}, and k_{geo} serves only to interpret them, for example through the position of the neutral axis that a given value of k_{eff} implies.

The applicability of this transformation is bounded by the assumptions of the shape function. Both beams tested in this study are simply supported, and for that condition a single half sine wave is a first-order approximation to the dominant symmetric component of the static deflected shape under quasi-static point or patch loading. It is not the exact static solution, since under a central point load the exact deflected shape of a simply supported beam is piecewise cubic and the curvature piecewise linear. Where the support condition differs, for example in a fixed-ended member or a beam continuous over several spans, the static shape contains curvature reversals that a single symmetric function cannot represent, and the three measurement points used here would not resolve them. Extension to such members requires a shape basis assembled from span-wise functions together with additional channels placed near the interior supports, where the curvature changes sign. Truncation of that basis, departure of the real boundary restraint from the assumed condition, and load distributions that differ appreciably from the case used for calibration each introduce error in the estimated displacement. Measurement noise is less critical, because the least squares solution over three channels averages the independent noise of the individual channels rather than propagating that of a single reading. Where a single channel is used, as in the large-scale test, the noise of that reading is reduced instead by averaging over the acquisition window. The three measurement points used in the laboratory reconstruction are not the mathematical minimum for a single-mode fit, which is one point, as used in the large-scale reconstruction of Sect. 5. They provide an overdetermined least squares estimate of the single modal amplitude, which limits the influence of any one channel. Additional measurements may be required as more modes are retained, depending on the rank and conditioning of the strain mode-shape matrix and on the sensor locations. The magnitude of the shape-function idealization can be stated analytically for the laboratory configuration. Under a central point load the exact normalized curvature at L/4, L/2 and 3 L/4 is 0.5, 1 and 0.5, whereas the half sine basis gives 0.707, 1 and 0.707. Converting from the mid-span strain alone through the half sine relation therefore overestimates the mid-span displacement by the factor $12/\pi^2$, or approximately 21.6%, relative to the exact Euler–Bernoulli solution, while a least squares fit of the same basis to all three measurement locations reduces the analytical bias to approximately 3.8%. These figures are a sensitivity benchmark for the assumed shape and are not an attribution of the discrepancies measured in Sect. 4. They apply to the geometric coefficient k_{geo}, since the effective coefficient k_{eff}, established by reference measurement, absorbs a uniform bias of this kind for the load configuration used to fix it.

The “Beam Structure” block defines the geometry and mesh of the beam, including dimensions, self-weight, and material properties, and generates a simple meshed 3D model. The “Visualization” block then represents the computed displacement through deflected geometry and color contours, where red, blue, and green indicate maximum, minimum, and intermediate displacements, respectively. Because the extremes of the mapping are defined by the maximum and minimum of the displacement field itself, the scale is relative to each update, so the colors describe the distribution within a single measurement rather than an absolute magnitude comparable between successive updates. For assessment against a serviceability criterion, or for a display refreshed continuously under moving load, the

Content courtesy of Springer Nature, terms of use apply. Rights reserved.

scale would instead be anchored to a fixed limit such as a project-specific or code-specified permissible deflection, so that a given color corresponds to the same physical condition on every update.

This BIM-based framework provides a practical solution for linking cloud-stored strain data with 3D structural visualization. Although simplified compared to a full BIM system, it demonstrates how MSVS data can be integrated into a digital environment for monitoring and decision support.

4 Lab-scale validation of MSVS

The performance of MSVS was first validated through a laboratory-scale experiment. A simply supported steel beam, 2 m in length, was placed on a carrier table and subjected to mid-span loading using weights of 20 lb (88.96 N) and 40 lb (177.93 N). Three pairs of strain gauges (active and dummy) were installed at the bottom of the beam at L/4, L/2, and 3 L/4 to form the three measurement channels of MSVS. A laser displacement sensor (LDS, optoNCDT ILD-1420) [63] was positioned at mid-span to provide reference displacement measurements, as shown in Fig. 8.

MSVS ADCs were operated at a sampling rate of 20 SPS, while the LDS sampled continuously at 1000 SPS. Prior to loading, initial strain measurements were acquired to remove offsets. MSVS was activated via push button, recording each channel for approximately 10 s (200 samples), while the LDS simultaneously measured displacement. The ADC gain was set to 1, and a strain calibration factor of 576 was applied to all channels. Here, the calibration factor was determined from the excitation voltage and gauge factor (GF = 2.1) according to the theoretical relationship between differential voltage and strain. This relationship is given by Eq. (2), and the same calibration factor was used in the single-channel implementation that preceded the present work [44]. The calibration factor is quoted here in με/mV, consistent with Eq. (2).

Under 20 lb. load, the LDS recorded a displacement of 0.40 mm, while MSVS measured strains of 73.89 με, 179.18 με, and 67.78 με for channels 1, 2, and 3, respectively. This case was used to calibrate the effective coefficient k_{eff} through Eq. (9), so the reconstructed displacement equals the LDS reading of 0.40 mm by construction and the case serves for calibration rather than as a check. When the beam was loaded with 40 lb., the LDS measured a displacement of 0.73 mm, and the corresponding strains recorded by MSVS were 219.05 με, 250.22 με, and 183.00 με. With the coefficient unchanged, Eq. (8) returns 0.77 mm for this case, which exceeds the LDS reading by 0.04 mm, or approximately 5%. The 40 lb case is therefore the independent comparison of the laboratory test. The results are summarized in Table 3.

Table 3 Lab-scale validation results (the 20 lb case calibrates the effective coefficient k_{eff} of Eq. (9))

Load (lb)	Ch1 Strain (με)	Ch2 Strain (με)	Ch3 Strain (με)	LDS (mm)	MSVS (mm)
20	73.89	179.18	67.78	0.40	0.40
40	219.05	250.22	183.00	0.73	0.77

The difference at the 40 lb case arises from several sources. Bonding of the gauge introduces a small multiplicative error in the measured strain through misalignment and the compliance of the adhesive layer, of which the part common to all channels is absorbed when the coefficient is fixed against the reference, whereas differences between channels alter the measured strain distribution and propagate into the estimated displacement. Conversion noise and quantization in the acquisition chain set a lower bound on strain precision that is independent of the other terms. Idealization of the mode shape contributes a bias, since the half sine is an approximation rather than the exact static solution for a central point load, and that bias grows where the supports carry rotational restraint or the load is not exactly centered. For the geometric coefficient k_{geo} the analytical benchmark of Sect. 3.2 places this term at approximately 3.8% for the three-point fit. With the coefficient fixed against the reference at 20 lb, a bias of this kind is absorbed for that load configuration, and only the departure of the 40 lb case from it contributes. The reference instrument contributes its own uncertainty, bounded by the linearity specified for the laser displacement sensor [63]. The alignment in time between the two acquisition systems contributes a further term. No one of these terms is identified as dominant, since neither the installation tolerance of the individual gauges nor a complete uncertainty budget for the reference instrument was recorded. The difference of 0.04 mm is therefore reported as the combined discrepancy of the whole measurement and reconstruction chain, rather than as an error attributable to MSVS alone, and it rests on a single independent load case. Because the reconstruction is linear, an error in the coefficient itself, including any error in the reference reading used to fix it, propagates in direct proportion into the estimated displacement. A quantitative propagation of these terms requires the installation tolerance of the individual gauges and is left to further work.

Following each measurement, the QR code displayed on the EPD was scanned using the developed Android application. The application decoded the content, converted it into a JSON object, and uploaded it to the cloud database via a REST API, demonstrating the acquisition, transfer and storage path of MSVS.

Content courtesy of Springer Nature, terms of use apply. Rights reserved.

5 Evaluation of MSVS at a large scale

To further evaluate the effectiveness of MSVS, a large-scale static load test was conducted on a composite steel–concrete beam at the POSCO Global R&D Centre, Incheon, South Korea. The aim was to validate MSVS under complex, less-controlled conditions and to verify its applicability for large-scale monitoring. The tested beam was 5.45 m in length, and two MSVS units were deployed, each connected to three strain channels located at L/4, L/2, and 3 L/4 along the span (channels 1, 2, and 3, respectively), one reading gauges on the steel section and the other gauges in the concrete, which were damaged when the concrete was cast. The results reported here are from the unit reading the steel gauges. The experimental setup is illustrated in Fig. 9.

The two validation cases were selected to advance from a controlled configuration to a representative one across three attributes at the same time. The span increases from 2 m to 5.45 m and the applied load from less than 200 N to 1300 kN. The section changes from a homogeneous steel member to a composite steel and concrete member, which alters the position of the neutral axis and the flexural stiffness entering the strain-to-displacement transformation. The acquisition method also changes, from scanning by hand indoors against a laser reference to periodic photography of the display in an industrial test hall against a linear variable differential transformer. Agreement with the reference measurement in both cases therefore provides evidence that the measurement chain can be applied across a substantial shift in scale, material and read-out method rather than being tuned to a single configuration. It is not claimed on this basis that a coordinated multi-unit pipeline has been demonstrated.

The beam was loaded using a universal testing machine up to a maximum static force of 1300 kN. Data were acquired every 5 min at a sampling rate of 20 SPS. The ADC gain and strain calibration factor were set to 1 and 576, respectively, and each channel was recorded for approximately 10 s (200 samples). An LVDT was installed at mid-span, coincident with strain channel 2, to serve as a reference displacement sensor, and a time-lapse camera was used to record the QR codes generated by MSVS for subsequent decoding and analysis. The measured strain responses are presented in Fig. 10.

The test consisted of two loading phases. In the first phase (Case 1), the load was gradually increased and held at a constant level for more than 10 min. In the second phase (Case 2), the load was further increased to the maximum before being gradually released. The maximum strain measured at mid-span (channel 2) reached 732.2 με. Displacements were reconstructed with the half sine relation of Eq. (8) applied to the mid-span channel alone ($n = 1$), which lies at the position of the LVDT, and are compared with the LVDT reference values in Fig. 11. The LVDT recorded maxima of 9.35 mm in Case 1 and 12.65 mm in Case 2. The effective coefficient k_{eff} was calibrated through Eq. (9) with the Case 1 maximum as the reference displacement, which gives approximately 56,300 microstrain per meter, and Case 2 then provides the independent comparison: the reconstruction of 13.01 mm at the Case 2 peak compares with 12.62 mm recorded by the LVDT at the same instant, a difference of 0.39 mm or 3.1%. This figure is a pointwise comparison at the instant of the MSVS peak; it is not a comparison with the LVDT maximum of 12.65 mm, which was recorded at a different instant, nor the largest difference over the loading and unloading history. Applying Eq. (8) to all three channels, with the coefficient fixed in the same way, changes the Case 2 estimate by less than 1%, since the ratio of the quarter-point to the mid-span strains changed little between the two cases (Fig. 10). Up to the Case 2 peak no reading differed from the simultaneous LVDT reading by more than 0.39 mm, but during unloading the reconstruction fell increasingly below the LVDT, by up to 1.17 mm at the last reading, when the LVDT still indicated 4.05 mm (Fig. 11). The cause was not established. An offset in time between the two records, which has most effect where the displacement changes fastest, and a residual deformation of the beam that the gauges do not register would each produce a difference of this sign, and neither was measured.

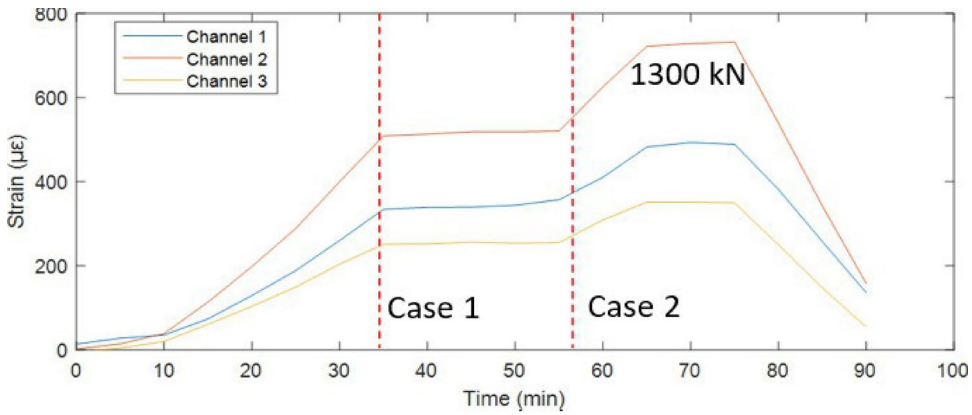


Fig. 10 Measured strains

Content courtesy of Springer Nature, terms of use apply. Rights reserved.

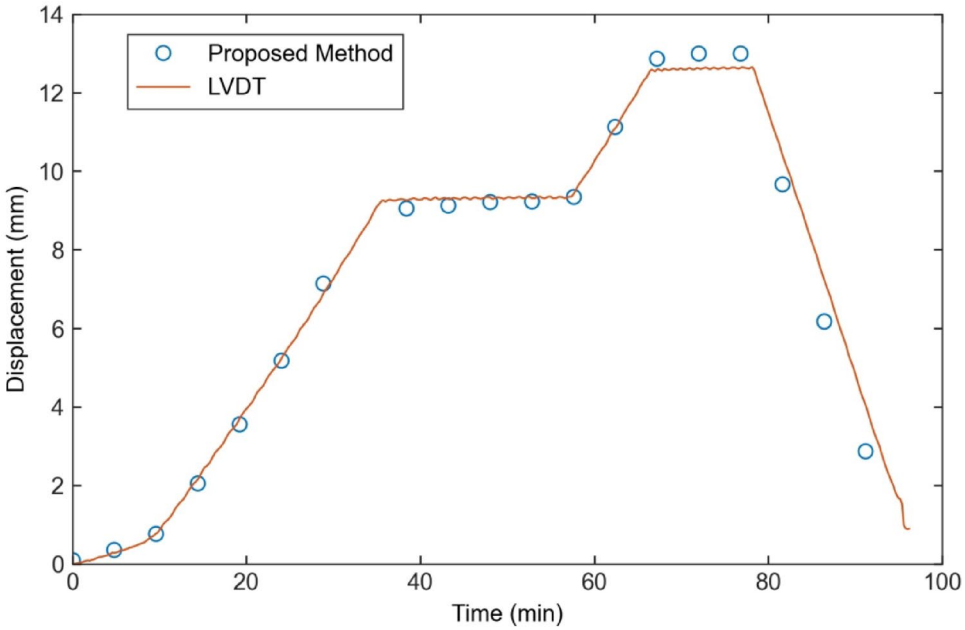


Fig. 11 Beam displacement

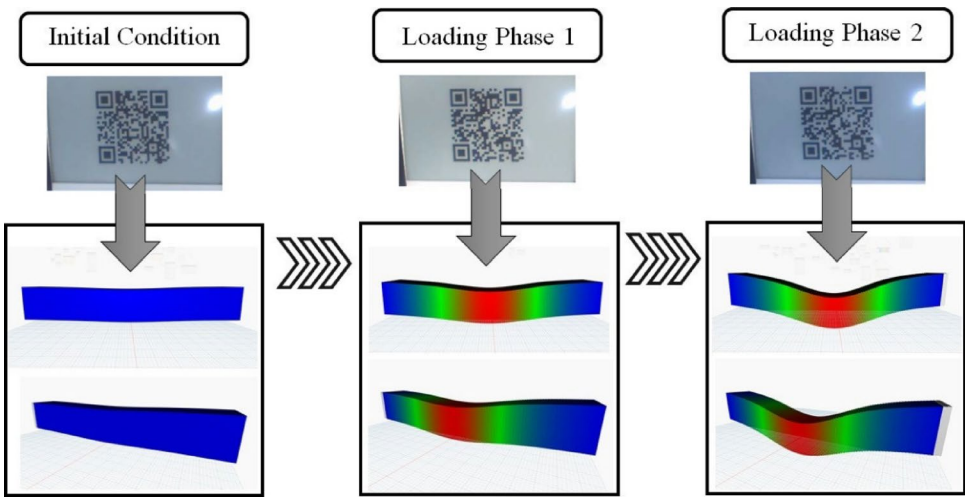


Fig. 12 QR code image and BIM-based visualization of beam

The comparison reported for the large-scale test is therefore limited to the loading phases and the peak.

Figure 12 presents examples of QR code images of the unit reading the steel gauges, captured by the time-lapse camera during the test, together with examples of the BIM-based visualization of the beam deflection. The visualization highlights displacement distribution through color contours, where red indicates maximum displacement and blue indicates minimum. These results indicate that MSVS can provide strain-based displacement estimation and visualization at the scale of this test.

6 Conclusion

This study proposed a novel multi-channel strain sensing and visualization system (MSVS) for long-term structural health monitoring. MSVS integrates low-power strain measurement, QR code–based data encoding, cloud-based data management, and BIM-based visualization into a compact and efficient platform. Key features include a power management circuit for ultra-low energy consumption and an EPD that enables visualization of strain data without continuous power. Within the classification adopted in Sect. 1, the platform provides the sensing and visualization layer on which a digital twin is built rather than a digital shadow, since in both experiments reported here the displayed record was captured manually or decoded from images after the event rather than transferred automatically.

Content courtesy of Springer Nature, terms of use apply. Rights reserved.

The system was validated through both laboratory- and large-scale experiments. In a 2 m simply supported beam test the displacement reconstructed at the validation load was within 0.04 mm, approximately 5%, of the laser reference, and for a 5.45 m composite beam under static loading up to 1300 kN the displacement reconstructed at its peak in the independent load case differed by 3.1% from the LVDT reading at the same instant. Because the strain-to-displacement coefficient was established against the reference in each test, each comparison rests on a single independent load case. The large-scale figure is a comparison at one instant, and the difference was larger during unloading, for reasons that were not established in this study. These results indicate that MSVS provides consistent strain sensing and displacement reconstruction across the two scales tested.

Despite its effectiveness, several limitations remain. The rendered size of the QR code is restricted by the memory required for the display buffers, and adopting higher QR code versions could increase capacity at the expense of module size and hence recognition reliability. Furthermore, while short-term validation was successful, full-scale long-term deployment is still required to verify durability and power efficiency. Future work will therefore focus on optimizing QR code encoding strategies and conducting extended field validation, including planned tests on a long-span bridge girder.

The sources of error in the complete measurement chain can be grouped by the stage at which they arise. In the sensing stage they comprise the bonding tolerance of the gauge, which introduces a small multiplicative error through misalignment and the compliance of the adhesive layer, conversion noise and quantization in the converter, and residual thermal effects, which the pairing of an active gauge with a dummy gauge in the half bridge compensates to first order in the thermal output of the gauges themselves. In the encoding and transfer stage the error correction carried by the code makes a corrupted record improbable once an image has been decoded, so the exposure at this stage is one of availability rather than accuracy: an image captured at an unfavorable angle or in insufficient light fails to decode and the record is deferred to the next attempt. In the displacement stage the terms are the idealization of the shape function, the uncertainty of the coefficient established against the reference instrument, the uncertainty of that instrument itself, and the alignment in time between the two systems. No single term is identified as dominant. The difference reported at the laboratory validation load is therefore the combined discrepancy between the two instruments, and a quantitative propagation of these terms awaits the gauge installation tolerances noted in Sect. 4.

The scope within which these results hold should be stated explicitly. The system was validated on simply supported members under quasi-static loading applied in steps. The acquisition scheme, which averages samples taken at 20 SPS over a short window at each activation, is directed at slow changes in deflection and does not resolve the dynamic response induced by traffic, which would require continuous or event-triggered acquisition at a rate appropriate to the frequency range of the structure, together with appropriate anti-alias filtering. Extension to dynamic monitoring would require an event-triggered mode, in which a low-power threshold detector arms a short burst of continuous sampling that is buffered and reduced to summary quantities before encoding, since a sampled waveform exceeds the capacity of the code adopted here. Such a mode raises the duty cycle and shortens the service life given in Sect. 2.3.

The architecture also governs the way the system scales. Platforms that transmit continuously are limited in node count by the capacity of the radio link and by the base station serving it. Each MSVS unit is self-contained and transmits nothing, presenting its result only as an image held on the display, so adding units to a structure adds neither radio traffic nor base station load. This shifts the principal constraint on scale rather than removing it. The number of units that can be deployed is then governed by the logistics of collecting the images, by line of sight and physical access to the displays, by the identification of individual units, and by the capacity of the database. Collection in the present form relies on an operator photographing the display during a site visit, which is possible because the display retains the code without power between activations. Unattended operation at higher frequency would require a fixed camera or an aerial platform triggered on the same schedule as the sensing event.

Further work will therefore address the extension of the shape basis to continuous and restrained members, the addition of transport security and offline buffering to the data path, an event-triggered mode for dynamic response, and long-term exposure of the display and the battery under outdoor conditions.

Funding This work was supported by the National Research Foundation of Korea (NRF) grant funded by the Korea government (MSIT) (RS-2025-02216760).

Data availability The datasets generated during and/or analyzed during the current study are available from the corresponding author on reasonable request.

Declarations

Conflict of interest The authors have no conflicts of interest.

Content courtesy of Springer Nature, terms of use apply. Rights reserved.

References

1. Sony S, Laventure S, Sadhu A (2019) A literature review of next-generation smart sensing technology in structural health monitoring. Struct Control Health Monit 26(3):e2321
2. Güemes A, Fernandez-Lopez A, Pozo AR, Sierra-Pérez J (2020) Structural health monitoring for advanced composite structures: a review. J Compos Sci 4(1):13
3. Kralovec C, Schagerl M (2020) Review of structural health monitoring methods regarding a multi-sensor approach for damage assessment of metal and composite structures. Sensors 20(3):826
4. Farrar CR, Worden K (2007) An introduction to structural health monitoring. Philos Trans R Soc A: Math Phys Eng Sci 365(1851):303–315
5. Biezma MV, Schanack F (2007) Collapse of steel bridges. J Perform Constr Facil 21(5):398–405
6. Barthorpe RJ, Worden K (2020) Emerging trends in optimal structural health monitoring system design: from sensor placement to system evaluation. J Sens Actuator Netw 9(3):31
7. Valinejadshoubi M, Bagchi A, Moselhi O (2019) Development of a BIM-based data management system for structural health monitoring with application to modular buildings: case study. J Comput Civil Eng 33(3):05019003
8. Kim N-S, Cho N-S (2004) Estimating deflection of a simple beam model using fiber optic Bragg-grating sensors. Exp Mech 44(4):433–439
9. Kim S-W, Kang W-R, Jeong M-S, Lee I, Kwon I-B (2013) Deflection estimation of a wind turbine blade using FBG sensors embedded in the blade bonding line. Smart Mater Struct 22(12):125004
10. Liu H-l, Zhu Z-w, Zheng Y, Liu B, Xiao F (2018) Experimental study on an FBG strain sensor. Opt Fiber Technol 40:144–151
11. Kang L-H, Kim D-K, Han J-H (2007) Estimation of dynamic structural displacements using fiber Bragg grating strain sensors. J Sound Vib 305(3):534–542
12. Dos Reis J, Oliveira Costa C, Sá da Costa J (2018) Strain gauges debonding fault detection for structural health monitoring. Struct Control Health Monit 25(12):e2264
13. Won J, Song M, Kim G, Atinaja IG, Park J-W, Jeon H (2025) LAVOLUTION: tunable structured light for bridge displacement measurement. Measurement 242:115807
14. Xie K, Ning J, Wang Q, Yao H (2025) Deformation prediction during the construction of segmental bridges based on GA-SMO-SVM algorithm: an example of CFST arch bridge. J Civil Struct Health Monit 15(1):31–57
15. Zhang L, Lu T, Wang F, Xia Y (2025) Over 25-year monitoring of the Tsing Ma suspension bridge in Hong Kong. J Civil Struct Health Monit 15(1):263–283
16. Wang M, Ding Y, Zhao H (2022) Digital prediction model of temperature-induced deflection for cable-stayed bridges based on learning of response-only data. J Civil Struct Health Monit 12(3):629–645
17. Sun Z, Santos J, Caetano E, Oliveira C (2023) Interpreting cumulative displacement in a suspension bridge with a physics-based characterisation of environment and roadway/railway loads. J Civil Struct Health Monit 13(2):387–397
18. Maboudi M, Backhaus J, Mai I, Ghassoun Y, Khedar Y, Lowke D et al (2025) Very high resolution bridge deformation monitoring using UAV-based photogrammetry. J Civil Struct Health Monit. 1–20
19. Zhang W, Sun L, Sun S (2017) Bridge-deflection estimation through inclinometer data considering structural damages. J Bridge Eng 22(2):04016117
20. You R-Z, Yi T-H, Ren L, Li H-N (2023) Equivalent estimation method (EEM) for quasi-distributed bridge-deflection measurement using only strain data. Measurement 221:113492
21. Tian Y, Zhang Z, Wang X, Li W, Xu Y (2025) Icing monitoring of wind turbine blade based on fiber Bragg grating sensors and strain ratio index. Energies 18(16):4295
22. Xu Y, Lin C, Bao Y, Li H (2026) Deep graph learning for spatial-temporal group-correlated in-service performance prediction of transportation infrastructure system. Adv Eng Inform 74:104791
23. Lee Y, Blaauw D, Sylvester D (2016) Ultralow power circuit design for wireless sensor nodes for structural health monitoring. Proc IEEE 104(8):1529–1546
24. Jang S, Jo H, Cho S, Mechitov K, Rice JA, Sim S-H et al (2010) Structural health monitoring of a cable-stayed bridge using smart sensor technology: deployment and evaluation. Smart Struct Syst 6(5–6):439–459
25. Cheng L, Pakzad SN (2009) Agility of wireless sensor networks for earthquake monitoring of bridges. In: 2009 sixth international conference on networked sensing systems (INSS), IEEE, pp 1–4
26. Fu TS, Ghosh A, Johnson EA, Krishnamachari B (2013) Energy-efficient deployment strategies in structural health monitoring using wireless sensor networks. Struct Control Health Monit 20(6):971–986
27. Won J, Park J-W, Park J, Shin J, Park M (2021) Development of a reference-free indirect bridge displacement sensing system. Sensors 21(16):5647
28. Lynch JP, Loh KJ (2006) A summary review of wireless sensors and sensor networks for structural health monitoring. Shock Vib digest 38(2):91–130
29. Abdulkarem M, Samsudin K, Rokhani FZ, Rasid A MF (2020) Wireless sensor network for structural health monitoring: a contemporary review of technologies, challenges, and future direction. Struct health Monit 19(3):693–735
30. O'Connor S, Lynch JP, Gilbert A (2014) Compressed sensing embedded in an operational wireless sensor network to achieve energy efficiency in long-term monitoring applications. Smart Mater Struct 23(8):085014
31. Lee J-H, Cheon D-J, Yoon S-W (2019) Vibration measurements of footbridges using wireless MEMS sensor. J Korean Assoc Spat Struct 19(1):101–108
32. Spencer B Jr, Park J-W, Mechitov KA, Jo H, Agha G (2017) Next generation wireless smart sensors toward sustainable civil infrastructure. Procedia Eng 171:5–13
33. Kim JS, Kibble K, Kwon YN, Sohn K-S (2009) Rate-equation model for the loading-rate-dependent mechanoluminescence of SrAl 2 O 4: Eu 2+, Dy 3+. Opt Lett 34(13):1915–1917
34. Zhang H, Yamada H, Terasaki N, Xu C-N (2007) Ultraviolet mechanoluminescence from SrAl2O4: Ce and SrAl2O4: Ce, Ho. Appl Phys Lett 91(8)
35. Akiyama M, Nishikubo K, Nonaka K (2003) Intense visible light emission from stress-activated SrMgAl 6 O 11: Eu. Appl Phys Lett 83(4):650–652
36. Zhang H, Terasaki N, Yamada H, Xu C-N (2009) Blue light emission from stress-activated Sr 2 MgSi 2 O 7: Eu. Int J Mod Phys B 23(06n07):1028–1033
37. Chandra V, Chandra B (2011) Suitable materials for elastico mechanoluminescence-based stress sensors. Opt Mater 34(1):194–200
38. Xu J, Jo H (2015) Development of high-sensitivity and low-cost electroluminescent strain sensor for structural health monitoring. IEEE Sens J 16(7):1962–1968
39. SHERIDON N (1977) The gyricon-a twisting ball display. SID 77 Digest. https://image-ppubs.uspto.gov/dirsearch-public/print/downloadPdf/6492967

Content courtesy of Springer Nature, terms of use apply. Rights reserved.

40. Comiskey B, Albert JD, Yoshizawa H, Jacobson J (1998) An electrophoretic ink for all-printed reflective electronic displays. Nature 394(6690):253–255
41. Fleming R, Peruvemba S, Holman R, Ferguson S, Sadlik B, Johansson T (2018) 48-2: Electronic Paper 2.0: frustrated eTIR as a Path to Color and Video. In: SID Symposium digest of technical papers: Wiley Online Library, pp 630–632
42. Fleming R, Kazlas P, Johansson T, Beales G, Manna E, Porush V et al (2019) 36-3: Tablet-size eTIR display for low-power ePaper applications with color video capability. In: SID Symposium digest of technical papers: Wiley Online Library, pp 505–508
43. Suciu G, Vochin M, Diaconu C, Suciu V, Butca C (2016) Convergence of software defined radio: WiFi, ibeacon and epaper. In: 2016 15th RoEduNet conference: networking in education and research, IEEE, pp 1–5
44. Khan S, Won J, Shin J, Park J, Park J-W, Kim S-E et al (2021) SSVM: an ultra-low-power strain sensing and visualization module for long-term structural health monitoring. Sensors 21(6):2211
45. Kritzinger W, Karner M, Traar G, Henjes J, Sihn W (2018) Digital Twin in manufacturing: a categorical literature review and classification. IFAC-PapersOnLine 51(11):1016–1022
46. Adafruit Adafruit Feather nRF52840 Sense. https://www.adafruit.com/product/4516 (n.d.). Accessed
47. Analog Devices (2015) DS3231. https://www.analog.com/en/products/ds3231.html Accessed 03 Sept 2025
48. Texas Instruments (2005) Sn74aup1g58. https://www.ti.com/product/SN74AUP1G58 Accessed 03 Sept 2025
49. Texas Instruments (2023) SN74LVC1G04. https://www.ti.com/product/SN74LVC1G04 Accessed 03 Sept 2025
50. Microchip Technology (2023) MCP1725. https://www.microchip.com/en-us/product/MCP1725 Accessed 03 Sept 2025
51. Texas Instruments (2023) TPS22860. https://www.ti.com/product/TPS22860 Accessed 03 Sept 2025
52. Texas Instruments (2023) SN74LVC1G373. https://www.ti.com/product/SN74LVC1G373 Accessed 03 Sept 2025
53. Texas Instruments (2023) ADS1220. https://www.ti.com/product/ADS1220 Accessed 03 Sept 2025
54. Hashmi MU, Labidi W, Bušić A, Elayoubi S-E, Chahed T (2018) Long-term revenue estimation for battery performing arbitrage and ancillary services. In: 2018 IEEE International conference on communications, control, and computing technologies for smart grids (SmartGridComm), IEEE, pp 1–7
55. Waveshare Electronics EPD. https://www.waveshare.com/7.5inch-hd-e-paper-hat.htm (n.d.). Accessed
56. Amazon (2021) Amazon aws, ec2. https://aws.amazon.com/ko/ec2/?ec2-whats-new.sort-by=item.additionalFields.postDateTime&ec2-whats-new.sort-order=desc Accessed September 3 2025
57. Oracle Coporation: MySQL (2023) https://www.mysql.com Accessed 03 Sept 2025
58. Developers Android studio (2021) https://developer.android.com/studio?gclid=CjwKCAiAu8SABhAxEiwAsodSZBml0FKYOgBCGQfKFTnDg_ 6zAC9_YTsQrTXyZgzmo8HF7bO5tL-5OBoCKU4QAvD_BwE&gclsrc=aw.ds. Accessed 03 Sept 2025
59. INCORPORATED DW (2025) QRcode.com. https://www.qrcode.com/en/about/version.html
60. Google: Volley (2021) https://github.com/google/volley Accessed 03 Sept 2025
61. OpenJS Foundation (2021) Node.js. https://nodejs.org/en Accessed 03 Sept 2025
62. Park J-W, Sim S-H, Jung H-J (2013) Displacement estimation using multimetric data fusion. IEEE/ASME Trans Mechatron 18(6):1675–1682
63. micro-epsilon https://www.micro-epsilon.com/distance-sensors/laser-sensors/optoncdt-1420/?sLang=en (n.d.). Accessed

Publisher's note Springer Nature remains neutral with regard to jurisdictional claims in published maps and institutional affiliations.

Springer Nature or its licensor (e.g. a society or other partner) holds exclusive rights to this article under a publishing agreement with the author(s) or other rightsholder(s); author self-archiving of the accepted manuscript version of this article is solely governed by the terms of such publishing agreement and applicable law.

Content courtesy of Springer Nature, terms of use apply. Rights reserved.

Terms and Conditions

Springer Nature journal content, brought to you courtesy of Springer Nature Customer Service Center GmbH ("Springer Nature").
Springer Nature supports a reasonable amount of sharing of research papers by authors, subscribers and authorised users ("Users"), for small-scale personal, non-commercial use provided that all copyright, trade and service marks and other proprietary notices are maintained. By accessing, sharing, receiving or otherwise using the Springer Nature journal content you agree to these terms of use ("Terms"). For these purposes, Springer Nature considers academic use (by researchers and students) to be non-commercial.
These Terms are supplementary and will apply in addition to any applicable website terms and conditions, a relevant site licence or a personal subscription. These Terms will prevail over any conflict or ambiguity with regards to the relevant terms, a site licence or a personal subscription (to the extent of the conflict or ambiguity only). For Creative Commons-licensed articles, the terms of the Creative Commons license used will apply.
We collect and use personal data to provide access to the Springer Nature journal content. We may also use these personal data internally within ResearchGate and Springer Nature and as agreed share it, in an anonymised way, for purposes of tracking, analysis and reporting. We will not otherwise disclose your personal data outside the ResearchGate or the Springer Nature group of companies unless we have your permission as detailed in the Privacy Policy.
While Users may use the Springer Nature journal content for small scale, personal non-commercial use, it is important to note that Users may not:

1. use such content for the purpose of providing other users with access on a regular or large scale basis or as a means to circumvent access control;
2. use such content where to do so would be considered a criminal or statutory offence in any jurisdiction, or gives rise to civil liability, or is otherwise unlawful;
3. falsely or misleadingly imply or suggest endorsement, approval , sponsorship, or association unless explicitly agreed to by Springer Nature in writing;
4. use bots or other automated methods to access the content or redirect messages
5. override any security feature or exclusionary protocol; or
6. share the content in order to create substitute for Springer Nature products or services or a systematic database of Springer Nature journal content.

In line with the restriction against commercial use, Springer Nature does not permit the creation of a product or service that creates revenue, royalties, rent or income from our content or its inclusion as part of a paid for service or for other commercial gain. Springer Nature journal content cannot be used for inter-library loans and librarians may not upload Springer Nature journal content on a large scale into their, or any other, institutional repository.
These terms of use are reviewed regularly and may be amended at any time. Springer Nature is not obligated to publish any information or content on this website and may remove it or features or functionality at our sole discretion, at any time with or without notice. Springer Nature may revoke this licence to you at any time and remove access to any copies of the Springer Nature journal content which have been saved.
To the fullest extent permitted by law, Springer Nature makes no warranties, representations or guarantees to Users, either express or implied with respect to the Springer nature journal content and all parties disclaim and waive any implied warranties or warranties imposed by law, including merchantability or fitness for any particular purpose.
Please note that these rights do not automatically extend to content, data or other material published by Springer Nature that may be licensed from third parties.
If you would like to use or distribute our Springer Nature journal content to a wider audience or on a regular basis or in any other manner not expressly permitted by these Terms, please contact Springer Nature at

onlineservice@springernature.com